Optics Letters

Virtual histopathology with ultraviolet scattering and photoacoustic remote sensing microscopy

Nathaniel J. M. Haven,[1,†] Matthew T. Martell,[1,†] Brendyn D. Cikaluk,[1] Brendon S. Restall,[1] Ewan McAlister,[1] Sveta Silverman,[2] Lashan Peiris,[3] Jean Deschenes,[2] Xingyu Li,[1] and Roger J. Zemp[1,*]

[1]Department of Electrical and Computer Engineering, University of Alberta, 116 Street & 85 Avenue, Edmonton, Alberta T6G 2R3, Canada
[2]Department of Laboratory Medicine and Pathology, University of Alberta, 116 Street & 85 Avenue, Edmonton, Alberta T6G 2R3, Canada
[3]Department of Surgery, University of Alberta, 116 Street & 85 Avenue, Edmonton, Alberta T6G 2R3, Canada
*Corresponding author: rzemp@ualberta.ca

Received 9 July 2021; revised 19 August 2021; accepted 19 August 2021; posted 20 August 2021 (Doc. ID 436136); published 7 October 2021

Realistic label-free virtual histopathology has been a long sought-after goal not yet achieved with current methods. Here, we introduce high-resolution hematoxylin and eosin (H&E)-like virtual histology of unstained human breast lumpectomy specimen sections using ultraviolet scattering-augmented photoacoustic remote sensing microscopy. Together with a colormap-matching algorithm based on blind stain separation from a reference true H&E image, we are able to produce virtual H&E images of unstained tissues with close concordance to true H&E-stained sections, with promising diagnostic utility.

https://doi.org/10.1364/OL.436136

The primary treatment for many solid cancers is tumor resection, where surgeons attempt to resect all cancerous tissue from the patient while conserving the surrounding healthy tissue. The boundaries of these excised specimens must then be inspected to verify clear margins. Currently, the histopathological assessment gold standard involves formalin-fixation, paraffin-embedding (FFPE), and hematoxylin and eosin (H&E) staining of these tissues before being reviewed by a pathologist using bright-field microscopy. Unfortunately, due to both the time-consuming and labor-intensive nature of this routine processing, histological interpretation is performed postoperatively. This delay in margin assessment can result in unnecessary additional surgeries, leading to worsened patient prognosis, as well as avoidable emotional and physical trauma. Consequently, there is an unmet need to develop a solution that can replace traditional FFPE H&E histopathological assessment by imaging resected tissue directly, within an intraoperative setting.

A literature review reveals a number of approaches that move towards this goal. Frozen section analysis (FSA) still relies on H&E staining, but bypasses some of the more time-consuming FFPE processing steps by rapidly freezing tissue. This technique is currently the standard of care; however, it struggles in lipid-rich tissues such as breast tissue, where freezing artifacts become prevalent [1]. Microscopy with ultraviolet surface excitation (MUSE) has demonstrated fast surface imaging of tissue samples, but suffers from non-uniform, tissue-dependent ultraviolet (UV) penetration depth, and requires the use of exogenous labels [2]. UV photoacoustic microscopy (UV-PAM) has shown impressive hematoxylin-like contrast from cell nuclei [3], but it relies on more complex setups to capture eosin-like contrast [4] and requires direct acoustic coupling to the sample, further complicating imaging procedures. Stimulated Raman scattering (SRS) has additionally demonstrated sub-cellular contrast of tissues, though it needs expensive ultrafast lasers [5].

We recently introduced UV photoacoustic remote sensing (UV-PARS) microscopy, which differs from UV-PAM in that it uses an additional interrogation beam to probe absorption-induced refractive index perturbations via the detection of backscattered modulations in this interrogation beam intensity. Using this imaging approach, we were first to demonstrate cell nuclei imaging by tuning the excitation wavelength to match an absorption peak of nucleic acids [6,7]. Additional work using UV-PARS has also been demonstrated by other groups [8]. However, these approaches have been able to provide only hematoxylin-like contrast of cell nuclei, omitting eosin-like contrast of the cytoplasm, which is important for a complete virtual H&E image. Recent advances have attempted to rectify this absence. Bell *et al*. used 420 nm excitation to target cytochromes to extract cytoplasm contrast [9]. Kedarisetti *et al*. recently presented a frequency-domain technique called f-mode PARS that was able to generate images with nuclear and cytoplasmic enhanced contrast using only a single excitation wavelength [10]. Additionally, Restall *et al*. first demonstrated the use of low-pass filtering on the existing near infrared (NIR) modulated backscattered interrogation beam signal to obtain eosin-corresponding scattering contrast [11]. This last method has also been recently demonstrated by Ecclestone *et al*. [12]. Of the two approaches presented that do not rely on additional excitation wavelengths, f-mode PARS is limited in that it struggles to extract cytoplasmic contrast when using low UV excitation powers, since any absorption in the cytoplasm is then greatly reduced and thus is not present in the resulting PARS signal. The method presented by Restall *et al*. [11] shows great

promise in simultaneously capturing scattering and UV-PARS data, since it provides a dual purpose for the NIR beam to capture both modulated and un-modulated backscattered light. However, one limitation of this system is that the resolution of the eosin-like image is significantly degraded in comparison to the hematoxylin-like UV-PARS image due to the longer NIR interrogation wavelength, limiting its utility to pathologists.

In this work, we demonstrate high-resolution virtual hematoxylin and eosin imaging of unstained human tissues with close concordance to true H&E-stained adjacent thin sections. To achieve this, we utilize UV scattering data as a virtual eosin channel while simultaneously capturing absorption data from UV-PARS as a virtual hematoxylin channel. A custom peak detection circuit is used to capture this pulsed UV scattering data. Furthermore, we introduce a novel algorithm to colormap match virtual H&E images obtained with our system to true H&E-stained reference images. These innovations allow us to showcase the first high-resolution, label-free, complete H&E-like images of human breast tissue.

Figure 1 shows the system diagram for the scattering-augmented UV-PARS setup. In the excitation pathway, a 20–600 kHz pulse repetition rate (PRR) linearly polarized 532 nm fiber laser (GLP-10, IPG Photonics) is used to provide a ns-pulsed excitation. The output of this laser is focused through a $5 \times 5 \times 6$ mm cesium lithium borate (CLBO) nonlinear crystal via a plano–convex lens (LA1464-A, Thorlabs) to obtain second harmonic generation (SHG) at 266 nm. The resulting beam is then re-collimated through a matching lens, and both the fundamental and SHG wavelengths are separated using a prism (PS863, Thorlabs). In the interrogation pathway, a 1319 nm linearly polarized superluminescent diode (SLD) (SLD1018PXL, Thorlabs) with single-mode fiber coupled output is collimated using a zoom collimator (ZC618APC-C, Thorlabs). Both the excitation and interrogation pathway beams are then expanded to a 5.1 mm diameter to fill the reflective objective input aperture. These beams then pass through independent half-wave plates (WPH05-1310, Thorlabs and WPH05M-266, Thorlabs) to rotate their linear polarization to match their respective polarizing beam splitter (CCM1-PBS254, Thorlabs and 10SC16PC.22, Newport) input polarizations. Prior to being combined via a harmonic beam splitter (HBSY134, Thorlabs), which transmits 1319 nm and reflects 266 nm, the beams are passed through independent quarter-wave plates (WPQ10M-1310, Thorlabs and WPQ10M-266, Thorlabs) to convert from linear to circular polarization. After combination, both beams are then co-aligned and co-focused through a 0.5 NA reflective objective (LMM-40X-UVV, Thorlabs) onto the sample. The backscattered excitation and interrogation beams change circular polarization handedness upon reflection, and thus are redirected from their respective incident beam paths via another pass through the quarter-wave plates and the polarization beam splitter cubes.

In the interrogation pathway, the continuous wave backscattered light is redirected onto a 75 MHz balanced photodiode (PDB420C-AC, Thorlabs). The RF output of this photodiode is used to detect modulations in the scattered light, corresponding to the PARS signal. This signal is further filtered using an in-line 20 kHz high-pass filter (KR Electronics) to remove scanning noise. The digital acquisition card is set to acquire 32 pre-trigger and 64 post-trigger data points at the 125 MS/s

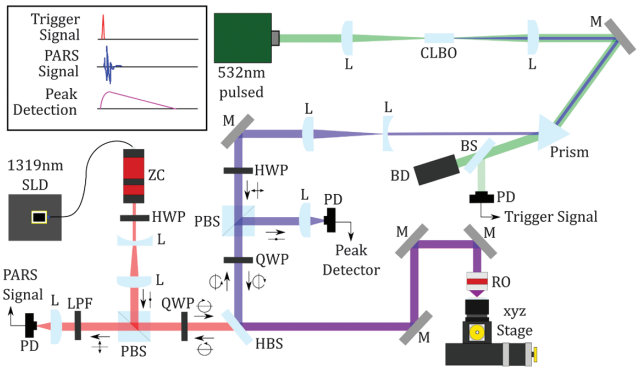

Fig. 1. UV Scattering-augmented UV-PARS setup: L, lens; BS, beam splitter; CLBO, cesium lithium borate crystal; M, mirror; HWP, half-wave plate; QWP, quarter-wave plate; LPF, longpass filter; PBS, polarizing beam splitter; PD, photodiode; RO, reflective objective; ZC, zoom collimator; BD, beam dump; HBS, harmonic beam splitter.

sampling rate to ensure the modulation peak is captured. To obtain the NIR scattering contrast simultaneously, a 100 kHz low-pass filter (KR Electronics) is used to remove the majority of the modulation from the secondary monitor photodiode output.

In the excitation pathway, a 150 MHz fixed gain photodiode (PDA10A, Thorlabs) is used to detect the backscattered pulsed UV beam. Since the pulse duration of the excitation laser is of the order of several nanoseconds, the digital acquisition card (CSE8389, Gage Applied), with a sampling rate of 125 MS/s, is unable to reliably sample this output. As a result, we utilized a custom peak detection circuit to hold the peak so that it can be sufficiently sampled by the card. The design of this circuit is detailed in Snider *et al*. [13].

To scan the samples, constant velocity stage scanning was utilized using a pair of linear $x - y$ stepper motor stages (PLS-85, PI) and their respective stage controllers (C-663, PI). The scanning protocol is described in more detail in Martell *et al*. [14], though burst mode of the digital delay generator was additionally used to allow finer 500 nm spatial sampling while operating the fast axis stage at its maximum 20 mm/s speed.

To replicate the traditional H&E colormap in our obtained UV scattering and UV-PARS images, the following approach was taken. Stain separation was performed on a reference true H&E image to separate the hematoxylin- and eosin-stained regions, as shown in Fig. 2. It is important to note that the reference H&E image is used to generate only our separate H&E colormaps, and thus does not need to correspond to the input scattering and UV-PARS images. The stain separation was performed using a blind separation algorithm first introduced by Li and Plataniotis [15,16]. After stain separation, minimum variance quantization was applied to each stain-separated image to divide their respective RGB color cubes into sub-divisions, which were used to generate individual separate hematoxylin and eosin colormaps. Before applying these colormaps to the UV-PARS and UV scattering images, histogram matching was performed between the virtual and true data sets, and the resulting images were median filtered with a 2×2 kernel. A flat-field correction was also applied to the UV-PARS images to improve uniformity in the nuclei contrast across the images. This approach enables stain style matching to images from any

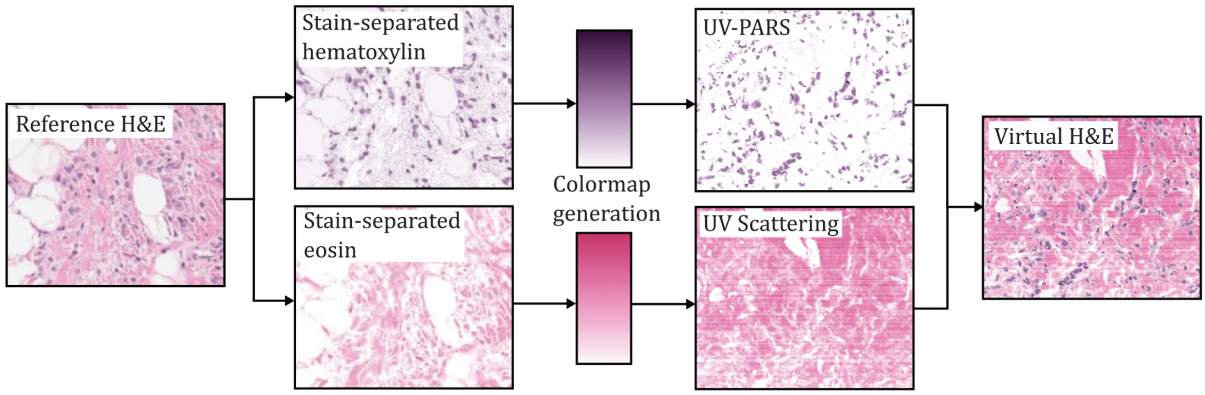

Fig. 2. Diagram showing the steps of the colormap-matching algorithm. Left: a reference H&E image is stain-separated into independent hematoxylin and eosin only images, these images are then used to generate hematoxylin and eosin colormaps. Right: these colormaps are applied to our separate UV-PARS and UV scattering images, which are then combined to generate a virtual H&E image.

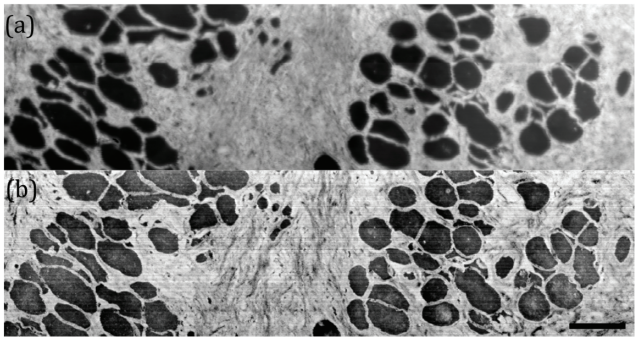

Fig. 3. Scattering images of human breast tissue using (a) CW NIR back-scattered light; (b) pulsed UV backscattered light. Scale bar: 100 μm.

pathology database, an important step towards preprocessing data for future artificial intelligence (AI) analysis.

Imaging of human breast lumpectomy specimens was then performed. Formalin-fixed, breadloafed lumpectomy specimens were obtained from breast cancer patients after pathology cases were closed and tissues were otherwise flagged for disposal as per approved ethics [HREBA (Cancer)/HREBA.CC- 20-0145]. Tissue sample patient information was redacted, and research staff and pathologists reading true and virtual H&E images were blinded to all patient and diagnostic information. Excised tissues were paraffin-embedded and sectioned into 4 μm thin sections, then de-paraffinated and covered in a thin layer of distilled water and a UV-transparent coverslip (CFQ-2220, UQG Optics) in preparation for UV-PARS imaging. For all imaging of tissues, a UV pulse energy of 2 nJ and NIR average power of 5 mW was co-focused onto the sample.

Resolutions of UV-PARS and NIR scattering have previously been determined to be 0.39 μm and 2.4 μm, respectively [11]. The UV scattering resolution is identical to the UV-PARS resolution. Comparing Figs. 3(a) and 3(b) showing simultaneously captured NIR and UV scattering images of human breast tissue samples, respectively, it is obvious that UV scattering reveals much finer detail including tissue striations that are not visible in the NIR scattering image. This is expected due to the ∼5 times resolution improvement due to the use of 266 nm instead of 1319 nm as the scattering wavelength.

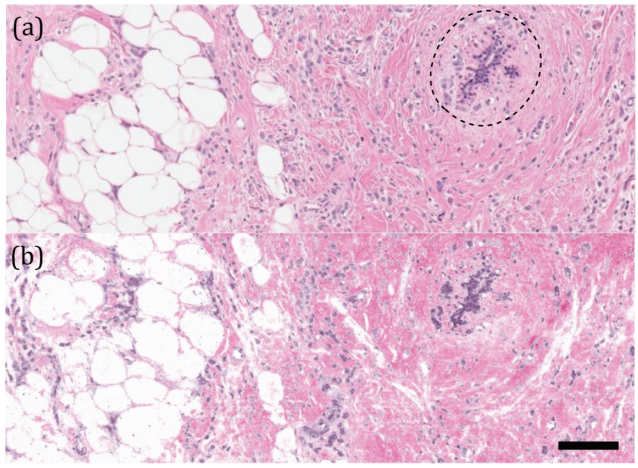

Fig. 4. Images of 4 μm sections of human breast lumpectomy specimens: (a) H&E-stained bright-field image; (b) colormap-matched combined UV scattering-augmented UV-PARS image, with the dashed region outlining a benign ductal structure. Scale bar: 100 μm.

Figure 4(b) showcases our colormap-matched UV scattering-augmented UV-PARS image of an unstained section from a human breast lumpectomy specimen, as compared to a true H&E-stained tissue section imaged under bright-field microscopy, as shown in Fig. 4(a). Comparing these images, strong concordance is evident. Differences between the images can be attributed to the samples being adjacent rather than identical sections from the same FFPE tissue block. Pathologist interpretation reveals invasive carcinoma cells arranged in cords and trabeculae, adjacent to fatty lobules, and minimal desmoplastic stromal response. Additionally, a benign ductal structure is indicated by the dashed region. Such diagnostic features are readily identifiable in the virtual image in addition to the true H&E image.

To evaluate the prospective utility of our virtual histopathology method, pathologists were asked to identify features of interest in a series of images of unstained sections of human breast lumpectomy specimens. Figure 5(a) was interpreted as exhibiting clear invasive carcinoma, with minimal desmoplastic response, some appreciation of the moderate cytological atypia associated with carcinoma, and invasion between fat cells

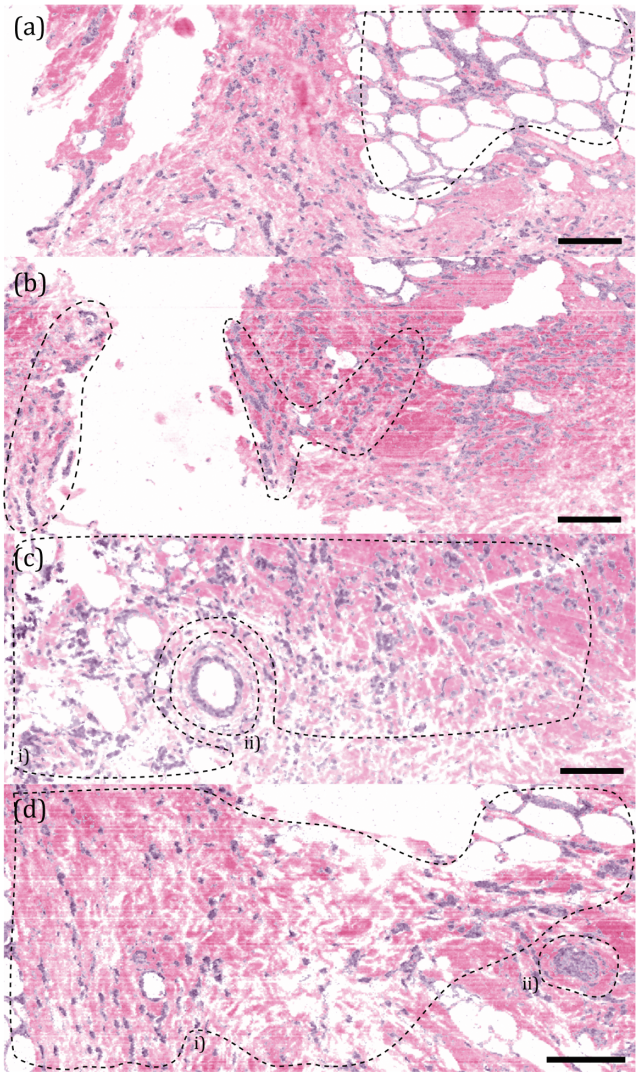

Fig. 5. (a)–(d) Pathologist-annotated UV scattering-augmented UV-PARS images of unstained sections of human breast lumpectomy specimens. Scale bars: 100 μm.

as shown in the dashed outline. In Fig. 5(b), dashed outlines emphasize regions where tumor cells are individually dispersed, non-cohesive, and arranged in a single file pattern with minimal desmoplastic response. Figure 5(c) shows invasive tumor cells with minimal desmoplastic stromal response, single file patterning, and small loose clusters in dashed region (i), and a benign duct can be seen in dashed region (ii). Finally, Fig. 5(d) also shows invasive carcinoma with minimal cytological pleomorphism and minimal desmoplastic response highlighted in dashed region (i), and dashed box (ii) highlights a potential ductal carconoma *in situ* (DCIS). The ability to visualize such histological characteristics in label-free images demonstrates strong potential as a diagnostic platform for pathologists.

Currently, a 2 mm × 0.5 mm image takes 13 min to acquire, with imaging speeds being limited by the stage scanning speed and the laser PRR. Future work should seek to improve on imaging speed to achieve utility for intraoperative applications. This should be readily possible. For example, using MHz excitation and optical scanning, a 1 cm × 1 cm image could be obtained in under 2 min. Parallelized readout could enable even faster imaging rates. Future work should also include assessing diagnostic concordance between pathologist interpretation of our virtual H&E images compared with true H&E stained images. Finally, we envision AI being used for rapid interpretation and flagging of areas for inspection by a pathologist.

In summary, by leveraging a stain-matching algorithm and introducing UV scattering as a high-resolution virtual eosin channel to augment absorption contrast from UV-PARS as a virtual hematoxylin channel, we have achieved realistic H&E-like virtual histological images of unstained human breast tissues. Our approach achieves close concordance to gold standard true H&E-stained images and demonstrates promising diagnostic utility in initial evaluations by pathologists.

Funding. Canadian Institutes of Health Research (PS 168936); Natural Sciences and Engineering Research Council of Canada (2018-05788).

Acknowledgment. The peak detection circuit used was originally designed by Logan Snider.

Disclosures. RJZ: IllumiSonics Inc. (I,P), CliniSonix Inc. (I,P), which, however, did not support this work.

Data Availability. Data available upon request.

[†]These authors contributed equally to this Letter.

REFERENCES

1. A. K. Glaser, N. P. Reder, Y. Chen, E. F. McCarty, C. Yin, L. Wei, Y. Wang, L. D. True, and J. T. Liu, Nat. Biomed. Eng. **1**, 0084 (2017).
2. F. Fereidouni, Z. T. Harmany, M. Tian, A. Todd, J. A. Kintner, J. D. McPherson, A. D. Borowsky, J. Bishop, M. Lechpammer, S. G. Demos, and R. Levenson, Nat. Biomed. Eng. **1**, 957 (2017).
3. D.-K. Yao, K. Maslov, K. K. Shung, Q. Zhou, and L. V. Wang, Opt. Lett. **35**, 4139 (2010).
4. C. Zhang, Y. S. Zhang, D.-K. Yao, Y. Xia, and L. V. Wang, J. Biomed. Opt. **18**, 020504 (2013).
5. D. A. Orringer, B. Pandian, Y. S. Niknafs, T. C. Hollon, J. Boyle, S. Lewis, M. Garrard, S. L. Hervey-Jumper, H. J. Garton, C. O. Maher, J. A. Heth, O. Sagher, D. A. Wilkinson, M. Snuderl, S. Venneti, S. H. Ramkissoon, K. A. McFadden, A. Fisher-Hubbard, A. P. Lieberman, T. D. Johnson, X. S. Xie, J. K. Trautman, C. W. Freudiger, and S. Camelo-Piragua, Nat. Biomed. Eng. **1**, 1 (2017).
6. N. J. Haven, K. L. Bell, P. Kedarisetti, J. D. Lewis, and R. J. Zemp, Opt. Lett. **44**, 3586 (2019).
7. N. J. Haven, P. Kedarisetti, B. S. Restall, and R. J. Zemp, Opt. Lett. **45**, 535 (2020).
8. S. Abbasi, M. Le, B. Sonier, D. Dinakaran, G. Bigras, K. Bell, J. R. Mackey, and P. H. Reza, Sci. Rep. **9**, 13392 (2019).
9. K. Bell, S. Abbasi, D. Dinakaran, M. Taher, G. Bigras, F. K. van Landeghem, J. R. Mackey, and P. H. Reza, Sci. Rep. **10**, 1 (2020).
10. P. Kedarisetti, B. S. Restall, N. J. Haven, M. T. Martell, B. D. Cikaluk, J. Deschenes, and R. J. Zemp, Opt. Lett. **46**, 3500 (2021).
11. B. S. Restall, N. J. Haven, P. Kedarisetti, M. T. Martell, B. D. Cikaluk, S. Silverman, L. Peiris, J. Deschenes, and R. J. Zemp, Opt. Express **29**, 13864 (2021).
12. B. Ecclestone, D. Dinakaran, and P. H. Reza, J. Biomed. Opt. **26**, 056007 (2021).
13. L. Snider, K. Bell, P. Hajireza, and R. J. Zemp, Proc. SPIE **10494**, 1049423 (2018).
14. M. T. Martell, N. J. Haven, and R. J. Zemp, J. Biomed. Opt. **26**, 066502 (2021).
15. X. Li and K. N. Plataniotis, IEEE J. Biomed. Health Inform. **21**, 150 (2017).
16. X. Li and K. N. Plataniotis, IEEE Trans. Biomed. Eng. **62**, 1862 (2015).